2012 Annual SCEC report

Numerical models of stress transfer from plate motion to mature transform faults

Publications and abstracts resulted from this project:

Takeuchi, C. and Y. Fialko, Dynamic models of interseismic deformation and stress transfer from plate motion to continental transform faults, J. Geophys. Res., 117, B05403, doi:10.1029/2011JB009056, 2012.

Takeuchi, C. and Y. Fialko, On the effects of thermally weakened ductile shear zones on postseismic deformation, J. Geophys. Res., submitted.

Takeuchi, C. and Y. Fialko, Lithospheric Shear Zones and Postseismic Deformation: Insights from 3-D Numerical Experiments, Abstract T31D-2625 presented at 2012 Fall Meeting, AGU, San Francisco, Calif., 3-7 Dec. 2012.

Summary of results:

We have extended 2-D anti-plane strain models of *Takeuchi and Fialko* (2012) to three dimensions to investigate effects of viscous shear zones that result from thermomechanical coupling on the geodetically observable deformation transients following an earthquake on a vertical strike-slip fault. We also explored potential kinematic similarities between viscoelastic models incorporating shear zones, and elastic models incorporating rate-strengthening friction on a deep aseismic fault root. We find that the thermally-activated shear zones have little effect on postseismic relaxation. In particular, the presence of shear zones does not change the polarity of vertical displacements in cases of rheologies that are able to generate robust postseismic transients. Stronger rheologies can give rise to an opposite polarity of vertical displacements, but the amplitude of the predicted transient deformation is generally negligible. We conclude that additional (to thermomechanical coupling) mechanisms of strain localization are required for a viscoelastic model to produce a vertical deformation pattern similar to that due to afterslip on a deep extension of a fault. We also investigated the discriminating power of models incorporating Burgers and power law rheology. These rheologies were proposed to explain postseismic transients following large ($M7$) earthquakes in the Mojave desert, Eastern California (e.g., *Freed and Bürgmann*, 2004; *Pollitz*, 2003). Numerical simulations indicate that it may be difficult to distinguish between these rheologies even with high-quality geodetic observations for observation periods less than a decade. Longer observations, however, may potentially allow discrimination between the competing models, as illustrated by the model comparisons with available GPS and InSAR data.

Technical report:

Large earthquakes are often followed by spatially- and temporally- varying deformation as the Earth's crust and mantle respond to stress perturbations produced by coseismic slip. Imaging of this transient deformation has dramatically improved in recent years as the density of GPS and InSAR observations has increased in both time and space around seismogenic faults. The primary mechanisms invoked to explain postseismic deformation include viscoelastic relaxation (*Elsasser*, 1969; *Nur and Mavko*, 1974; *Savage and Prescott*, 1978), aseismic fault creep (*Ruina*, 1983; *Tse and Rice*, 1986), and poroelastic rebound (*Booker*, 1974; *Jonsson et al.*, 2003). Poroelastic relaxation and shallow afterslip are upper crustal processes that have predominantly near-field effects, while deeper afterslip and viscoelastic relaxation occur mainly in the lower crust and upper mantle and thus produce broad-ranging surface displacements.

The individual contributions of these mechanisms to postseismic relaxation following a given event may be difficult to identify, largely due to the non-uniqueness of inverse models. For instance, for an infinitely long strike-slip fault undergoing uniform coseismic displacement, viscoelastic relaxation predicts surface deformation that is indistinguishable from that due to an appropriately configured elastic dislocation model (*Savage*, 1990). It was proposed that in the case of three-dimensional (3-D) deformation due to finite ruptures, the afterslip and viscoelastic relaxation mechanisms may in principle be distinguished as these mechanisms predict vertical postseismic velocity patterns that are opposite in polarity (e.g., *Pollitz et al.*, 2001). In addition, viscoelastic relaxation models typically predict relatively large fault-normal velocities up- and down-strike from a finite strike-slip rupture, while such velocities are small or absent in afterslip models (*Hearn*, 2003). However, if multiple mechanisms contribute to postseismic relaxation, even high-quality observations may not allow for robust discrimination between the candidate mechanisms. For example, postseismic deformation in the Eastern California Shear Zone (ECSZ) following the 1992 M_w7.3 Landers and 1999 M_w7.1 Hector Mine earthquakes has been ascribed to viscoelastic relaxation (*Pollitz*, 2003), (*Freed and Bürgmann*, 2004), a combination of poroelastic relaxation and afterslip (*Fialko*, 2004a; *Peltzer et al.*, 1998), poroelastic and viscoelastic relaxation (*Masterlark and Wang*, 2002), as well as other mechanisms (*Jacobs et al.*, 2002; *Massonnet et al.*, 1996).

Afterslip on the deep extension of the rupture plane may be considered to be kinematically analogous to a narrow ductile shear zone, with shear deformation governed by the constitutive equation for stress-driven frictional afterslip rather than that for viscoelastic flow (e.g., *Barbot et al.*, 2009). Several previous investigations of postseismic relaxation have allowed for strain localization in the viscoelastic medium by incorporating a tabular region of reduced effective viscosity along the fault root (e.g., *Freed et al.*, 2007; *Hearn et al.*, 2009; *Kenner and Segall*, 2003). However, the introduction of such shear zones into numerical models is usually *ad hoc* and neglects details of how such zones formed in the first place. In a previous study, we demonstrated that shear heating and thermomechanical coupling in the ductile substrate give rise to long-lived localized shear zones beneath mature strike-slip faults (*Takeuchi and Fialko*, 2012). These shear zones participate both in loading faults interseismically and relaxing coseismic stress perturbations. Here, we extend our 2-D results to 3-D finite-rupture scenarios. We use our models to test the hypothesis that, under assumptions of laboratory-derived rheologies and far-field loading, a model incorporating highly localized ductile shear zone produced by shear heating may produce a postseismic deformation field similar to that predicted by a frictional afterslip model. In this case, different patterns of

postseismic deformation might be expected depending on the effective fault age and slip rate, with afterslip-like localized viscoelastic shear dominating postseismic relaxation in the case of mature faults, and diffuse viscoelastic relaxation dominating in the case of immature faults. We find that, contrary to the hypothesis, thermally-induced shear zones have little effect on postseismic relaxation. It follows that the degree of shear localization necessary for a viscoelastic relaxation model to mimic postseismic surface deformation due to frictional afterslip model requires additional localization mechanisms.

Most of numerical simulations were carried out using the finite element software Abaqus/Simulia (www.simulia.com/products/abaqus_fea.html). The model domain is a 600 km (fault-normal, x coordinate) x 600 km (along-strike, y coordinate) x 75 km (vertical, z coordinate) rectangular block. The domain is composed of three horizontal rheological layers: a 12 km-thick elastic upper crust overlying an 18 km-thick viscoelastic lower crust and a 45 km-thick viscoelastic upper mantle. A 600 km-long (y = -300 to 300 km) vertical planar fault is introduced within the domain at $x = 0$. The fault penetrates through the entire upper crust and roots in the lower crust at a depth of 17 km.

The model domain is discretized into 612,000 elements, with 34 element layers in the fault-normal direction, 240 layers in the strike direction, and 75 vertical layers. Fault-normal node spacing decreases towards the fault, from 93.58 km in the far-field to 0.5 km on the fault. Along-strike node spacing varies from 19.57 km in the far-field to 0.5 km for $|y|$>35 km; nodes are spaced by 0.5 km within $|y|\leq$35 km. Nodes are spaced vertically by 1 km.

Rheology

We explored four candidate rheologies of the viscoelastic lower crust and upper mantle. Two models incorporate linear rheologies for these layers. The first model incorporates a Maxwell rheology for the entire ductile substrate. The mantle has a viscosity η_m of 1.6×10^{17} Pa s, corresponding to the transient rheology of *Pollitz* (2003), and a shear modulus μ_m of 70 GPa. The lower crust in this model has a viscosity η_c of 3.2×10^{19} Pa s and a shear modulus μ_c of 38 GPa. Poisson's ratio is 0.25 in all model layers. We refer to this model as MS.

The second model incorporating linear rheology assumes a biviscous Burgers body rheology, in which Maxwell and Kelvin viscoelastic elements are in series. The shear relaxation modulus for a Burgers rheology with steady-state and transient viscosities η_1 and η_2, respectively, and steady-state and transient shear moduli μ_1 and μ_2, respectively, is (*Findlay et al.*, 1989)

$$G_R(t) = \frac{1}{A}[(q_1 - q_2 r_1)\exp(-r_1 t) - (q_1 - q_2 r_2)\exp(-r_2 t)] \tag{1}$$

where

$$q_1 = 2\eta_1,\ q_2 = 2\frac{\eta_1\eta_2}{\mu_2},\ r_1 = \frac{p_1 - A}{2p_2},\ r_2 = \frac{p_1 + A}{2p_2}. \tag{2}$$

with

$$p_1 = \frac{\eta_1}{\mu_1} + \frac{\eta_1}{\mu_2} + \frac{\eta_2}{\mu_2},\ p_2 = \frac{\eta_1\eta_2}{\mu_1\mu_2},\ A = \sqrt{p_1^2 - 4p_2} \tag{3}$$

The shear relaxation modulus may be represented by a dimensionless Prony series expansion

$$g_R(t) = \frac{G_R(t)}{G_0} = 1 - \sum_{i=1}^{N} \bar{g}_i^P (1 - \exp(\frac{-t}{\tau_i^G})). \tag{4}$$

Table 1: Laboratory-derived material properties of rocks.

Rock Type	A (MPa^{-n} s^{-1})	n	Q (kJ mol^{-1})	ρ (kg m^{-3})	Ref.
Dry diabase	8.0	4.7	485	2850	1
Wet diabase	2.2×10^{-4}	3.4	260	2850	2
Dry olivine	1.1×10^{4}	3.5	535	3320	3
Wet olivine	3.6×10^{5}	3.5	480	3320	3

[1]*Mackwell et al.* (1998); [2]*Shelton and Tullis* (1981); [3]*Hirth and Kohlstedt* (2004)

by recognizing that if $C = (q_1 - q_2 r_1)/A$ and $D = (q_2 r_2 - q_1)/A$, equation 1 may be expressed as

$$G_R(t) = (C + D) - [C(1 - \exp(-r_1 t)) + D(1 - \exp(-r_2 t))]. \quad (5)$$

Normalizing by $G_0 = C + D$ yields the two-term dimensionless Prony series with $\bar{g}_1^P = C/(C + D)$, $\tau_1^G = 1/r_1$, $\bar{g}_2^P = D/(C + D)$, and $\tau_2^G = 1/r_2$.

We select Burgers body parameters $\eta_1 = 4.6 \times 10^{18}$ Pa s, $\eta_2 = 1.6 \times 10^{17}$ Pa s, $\mu_1 = 70$ GPa, and $\mu_2 = 70$ GPa, which were the best-fitting values of *Pollitz* (2003) for the rheology of the mantle beneath the Mojave Desert, California. We also use the best-fitting model of *Pollitz* (2003) for the lower crust, which incorporates a Maxwell rheology with a viscosity $\eta_c = 3.2 \times 10^{19}$ Pa s and a shear modulus $\mu_c = 38$ GPa (this value represents an average of the depth-varying shear modulus of *Pollitz* (2003) over our lower crustal depth range of 12-30 km). The lower crust for the biviscous-mantle model and the Maxwell-mantle model are thus identical. Poisson's ratio is 0.25 for all materials in the biviscous-mantle model. We refer to this model as BI.

The remaining two models incorporate non-linear, temperature-dependent rheology. In these models, the deviatoric strain rate $\dot{\varepsilon}_d$ and deviatoric stress σ_d in each finite element are related by the constitutive equation

$$\dot{\varepsilon}_d = A\sigma_d^n \exp(-\frac{Q}{RT}) \quad (6)$$

where R is the universal gas constant, and the power law pre-multiplier A, the stress exponent n, and the activation energy Q are empirically-determined constants (*Kirby and Kronenburg*, 1987). The constitutive relation yields a stress- and temperature-dependent effective viscosity η_{eff} for each finite element

$$\eta_{eff} = \frac{\sigma_d}{\dot{\varepsilon}_d} = \frac{1}{A\sigma_d^{n-1}} \exp(\frac{Q}{RT}). \quad (7)$$

We assume mafic (diabase) and ultramafic (olivine) composition for the lower crust and upper mantle, respectively (*Rudnick and Fountain*, 1995); (*Karato and Wu*, 1993). To account for variability in ductile strength, we consider end-member models of hydrated (weak) and dry (strong) mineral compositions. Laboratory-determined material parameters for these models are listed in Table 1. In all power law models, the elastic behavior of both the upper crust and the ductile substrate is governed by the linear isotropic Hooke's Law, with a shear modulus and Poisson's ratio of 32 GPa and 0.25, respectively.

Earthquake Simulations

In this study we employed kinematically-driven earthquake cycles, i.e. coseismic fault slip is prescribed as a boundary condition. Such models generate unphysical stresses in the lithosphere; in particular, repeated kinematically-prescribed earthquakes produce negative (i.e. having sense opposite to that of fault slip) stresses in the seismogenic layer (*Takeuchi and Fialko*, 2012). However, surface velocities are relatively insensitive to the type of boundary condition on a fault surface (*Takeuchi and Fialko*, 2012).

The models are "spun up" by prescribing creep on a fault in the upper crust and at the far sides of the model for 10 Ma, followed by ten earthquake cycles on the entire 600 km-long fault. In these cycles, we prescribe an instantaneous coseismic slip of 8 m on the upper 12 km of the fault. Fault slip is again cosine-tapered to zero at 17 km depth. We then lock the fault for an interseismic period of 200 years. The total relative plate velocity (40 mm/yr) is maintained on the far-field boundaries of the model domain for the duration of the earthquake cycle sequence. Because deformation is anti-plane strain, only fault-parallel motion is allowed.

Following the final interseismic period of the last system-wide earthquake, we simulate a finite rupture on a 70 km-long segment in the middle of the domain ($|y| \leq 35$ km). Slip amplitude is the same as in previous system-wide events. The respective moment is 1.08×10^{20} N m, similar to the moment estimates for the 1992 M_w7.3 Landers rupture (*Fialko*, 2004b; *Kanamori et al.*, 1992; *Sieh et al.*, 1993), and slightly higher than those for the 1999 M_w7.1 Hector Mine rupture (*Dreger and Kaverina*, 2000; *Simons et al.*, 2002).

We generate maps of postseismic velocity, from which contributions of secular deformation have been removed. We study the first 50 years of deformation, as postseismic velocities after this time are likely to fall below the detection limit, and there are few examples of geodetically documented long-lasting (>50 years) postseismic deformation transients. Figures 1-2 illustrate modeled postseismic surface velocities within 100 km of the fault for two epochs following coseismic rupture. Six months after the earthquake (Figure 1), each model shows a clear four-quadrant pattern of uplift and subsidence, though the polarity and amplitude of deformation varies. Model MS predicts the largest amplitudes of vertical velocity at this time epoch, as expected due to the short relaxation timescale of the substrate. Wet power law models all have similar vertical velocity patterns, though WFB has larger amplitudes and smaller wavelength lobes compared to models WNS and WSZ. Model DNS shows a similar pattern to the wet power law models, though amplitudes are an order of magnitude smaller, and relatively large vertical velocities are seen in the far-field. Model DSZ shows similar amplitudes and far-field polarity as DNS, but the near-field polarity is reversed relative to all other viscoelastic models. Model AFT (afterslip) is the only other model showing near-field subsidence northeast and southwest of the finite rupture, and uplift northwest and southeast of the rupture.

Horizontal velocities six months following the earthquake show broadly similar qualitative patterns for all models, with quadrant patterns of combined right-lateral fault-parallel velocities and left-lateral fault-perpendicular velocities.

Fifty years after the rupture, all models except DNS, WFB, and WNS demonstrate significant evolution of the respective surface velocity patterns (Figure 2). Vertical velocity lobes in model AFT have expanded significantly towards the far-field, reflecting propagation of afterslip towards deeper parts of the fault. Model BI predicts a low-amplitude reversed-polarity near-field vertical velocity pattern. Model DSZ shows significantly enhanced near-field vertical velocities relative to far-field

velocities, as well as reduced far-field fault-parallel velocity and negligible fault-parallel velocity up- and down-strike from the rupture. Model MS predicts expansion of the 10-year reversed polarity quadrant pattern towards the far-field. Model WSZ shows the initiation of a reversed near-field vertical pattern. Vertical velocities at this epoch are very small (<1 mm/yr), likely below the geodetic detection limits. However, models BI and MS maintain appreciable horizontal velocities, reflecting ongoing substrate response to coseismic stress changes even 50 years after the event.

Outreach and broader impacts:

This project provided training and support for one graduate student and one postdoc. The PI (Fialko) used results of this study in a graduate class taught at SIO.

References

Barbot, S., Y. Fialko, and Y. Bock, Postseismic deformation due to the *Mw* 6.0 2004 Parkfield earthquake: Stress-driven creep on a fault with spatially variable rate-and-state friction parameters, *J. Geophys. Res.*, *114*, B07405, doi:10.1029/2008JB005748, 2009.

Booker, J., Time dependent strain following faulting of a porous medium, *J. Geophys. Res.*, *79*(14), doi: 10.1029/JB079i014p02037, 1974.

Dreger, D., and A. Kaverina, Seismic remote sensing for the earthquake source process and near-source strong shaking: A case study of the October 16, 1999 Hector Mine earthquake, *Geophys. Res. Lett.*, *27*, 1,941–1,944, 2000.

Elsasser, W., Convection and stress propagation in the upper mantle,, in *The Application of Modern Physics to the Earth and Planetary Interiors*, edited by S. K. Runcom, Wiley-Interscience, London, 1969.

Fialko, Y., Evidence of fluid-filled upper crust from observations of postseismic deformation due to the 1992 Mw7.3 Landers earthquake, *J. Geophys. Res.*, *109*, B08401, doi:10.1029/2004JB002985, 2004a.

Fialko, Y., Probing the mechanical properties of seismically active crust with space geodesy: Study of the co–seismic deformation due to the 1992 Mw7:3 Landers (southern California) earthquake, *J. Geophys. Res.*, *109*, B03307, doi:10.1029/2003JB002756, 2004b.

Findlay, W., J. Lai, and K. Onaran, *Creep and Relaxation of Nonlinear Viscoelastic Materials*, 371 pp., Dover Publishing, New York, 1989.

Freed, A., and R. Bürgmann, Evidence of power–law flow in the Mojave desert mantle, *Nature*, *430*, 548–551, doi: 10.1038/nature02784, 2004.

Freed, A., R. Bürgmann, and T. Herring, Far–reaching transient motions after Mojave earthquakes require broad mantle flow beneath a strong crust, *Geo. Res. Lett.*, *34*, doi:10.1029/2007GL030959, 2007.

Hearn, E., What can GPS data tell us about the dynamics of post–seismic deformation?, *Geophys. J. Int.*, *155*, 753–777, doi:10.1029/JB095iB04p04873, 2003.

Hearn, E., S. McCluskey, S. Ergintav, and R. Reilinger, Izmit earthquake postseismic deformation and dynamics of the North Anatolian Fault Zone, *J. Geophys. Res.*, *114*, B08405, doi:10.1029/2008JB006026, 2009.

Hirth, G., and D. Kohlstedt, Rheology of the upper mantle and mantle wedge: A view from the experimentalists, in *Inside the Subduction Factory, Geophys. Monogr. Ser.*, vol. 138, edited by J. Eiler, pp. 83–105, AGU, Washington, D. C, 2004.

Jacobs, A., D. Sandwell, Y. Fialko, and L. Sichoix, The 1999 (*Mw*7.1) Hector Mine, California, earthquake: Near-field postseismic deformation from ERS interferometry, *Bull. Seism. Soc. Am.*, *92*, 1,433–1,442, 2002.

Jonsson, S., P. Segall, R. Pedersen, and G. Bjornsson, Post-earthquake ground movements correlated to pore-pressure transients, *Nature*, *424*, 179–183, 2003.

Kanamori, H., H. Thio, D. Dreger, E. Hauksson, and T. Heaton, Initial investigation of the Landers, California, earthquake of 28 June 1992 using TERRAscope, *Geophys. Res. Lett.*, *19*, 2,267–2,270, 1992.

Karato, S., and P. Wu, Rheology of the upper mantle: A synthesis, *Science*, *260*, 771–778, doi: 10.1126/science.260.5109.771, 1993.

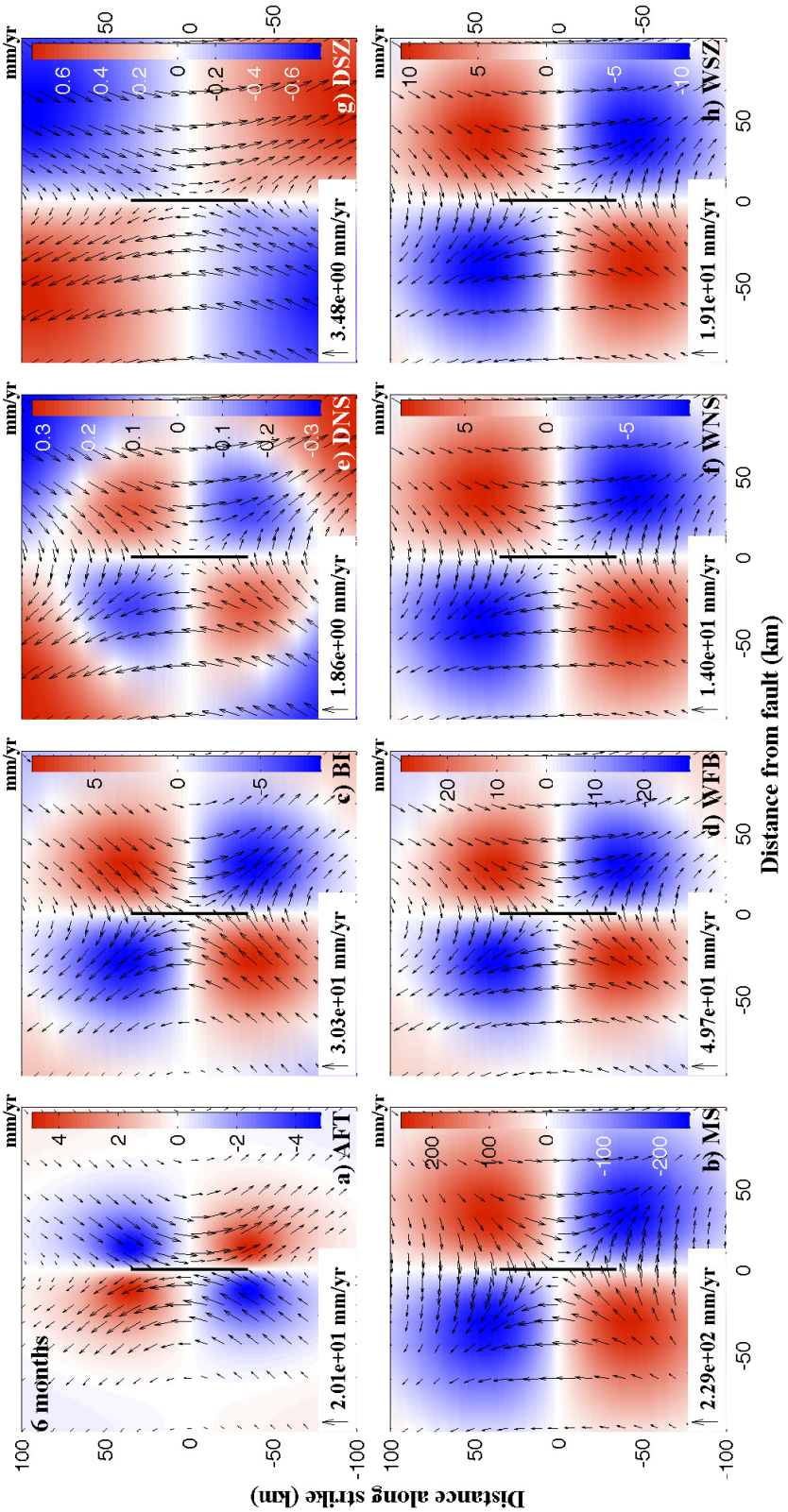

Figure 1: Map view of postseismic surface velocities in mm/yr, 6 months after rupture for models a) AFT (afterslip), b) MS (Maxwell), c) BI (biviscous), d) WFB (wet power law, *Freed and Bürgmann* (2004) thermal regime), e) DNS (dry power law, no shear zone), f) WNS (wet power law, no shear zone), g) DSZ (dry power law, shear zone), h) WSZ (wet power law, shear zone). Colors indicate vertical velocity, arrows indicate horizontal velocity (scales are indicated in each panel). Heavy black line denotes the fault plane.

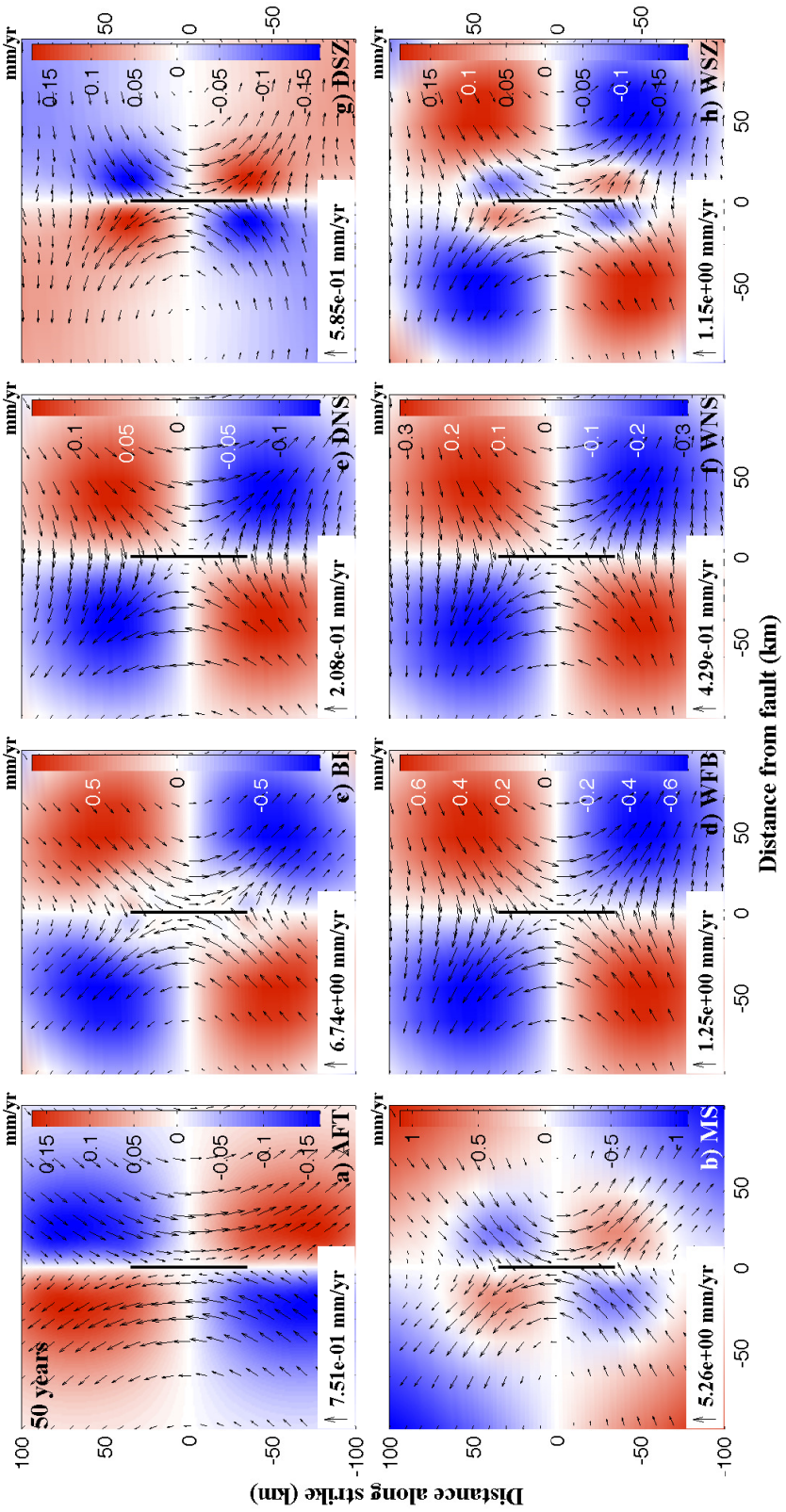

Figure 2: Postseismic surface velocities in mm/yr, 50 years after rupture. Panels as indicated in Figure 1 caption. Colors indicate vertical velocity, arrows indicate horizontal velocity. Heavy black line denotes the fault plane.

Kenner, S., and P. Segall, Lower crustal structure in northern California: Implications from strain rate variations following the 1906 San Francisco earthquake, *J. Geophys. Res.*, *108*(B1), doi:10.1029/2001JB000189, 2003.

Kirby, S., and A. Kronenburg, Rheology of the lithosphere: Selected topics, *Rev. Geophys.*, *25*, 1,219–1,244, 1987.

Mackwell, S., M. Zimmerman, and D. Kohlstedt, High-temperature deformation of dry diabase with application to tectonics on venus, *J. Geophys. Res.*, *103*, 975–984, doi:10.1029/97JB02671, 1998.

Massonnet, D., W. Thatcher, and H. Vadon, Detection of postseismic fault-zone collapse following the Landers earthquake, *Nature*, *382*, 612–616, 1996.

Masterlark, T., and H. Wang, Transient stress-coupling between the 1992 Landers and 1999 Hector Mine, California, earthquakes, *Bull. Seism. Soc. Am.*, *92*, 1,470–1,486, 2002.

Nur, A., and G. Mavko, Postseismic viscoelastic rebound, *Science*, *183*, 204–206, doi:10.1126/science.183.4121.204, 1974.

Peltzer, G., P. Rosen, F. Rogez, and K. Hudnut, Poro–elastic rebound along the Landers 1992 earthquake surface rupture, *J. Geophys. Res.*, *103*(B12), 30,131–30,145, 1998.

Pollitz, F., Transient rheology of the uppermost mantle beneath the Mojave Desert, California, *Earth Planet. Sci. Lett.*, *215*, 89–104, doi:10.1016/S0012-821X(03)00432-1, 2003.

Pollitz, F., C. Wicks., and W. Thatcher, Mantle flow beneath a continental strike–slip fault: Postseismic deformation after the 1999 Hector Mine earthquake, *Science*, *293*, 1,814–1,818, 2001.

Rudnick, R., and D. Fountain, Nature and composition of the continental crust: A lower crustal perspective, *Rev. Geophys.*, *33*, 267–309, doi:10.1029/95RG01302, 1995.

Ruina, A., Slip instability and state variable friction laws, *J. Geophys. Res.*, *88*, 10,359–10,370, 1983.

Savage, J., Equivalent strike-slip earthquake cycles in halfspace and lithosphere-asthenosphere Earth models, *J. Geophys. Res.*, *95*, 4,873–4,879, doi:10.1029/JB095iB04p04873, 1990.

Savage, J., and W. Prescott, Asthenosphere readjustment and the earthquake cycle, *J. Geophys. Res.*, *83*, 3,369–3,376, 1978.

Shelton, G., and J. Tullis, Experimental flow laws for crustal rocks, *Eos Trans. AGU*, *62*, 396, 1981.

Sieh, K., et al., Near–field investigations of the Landers earthquake sequence, April to July 1992, *Science*, *260*, 171–176, 1993.

Simons, M., Y. Fialko, and Y. Rivera, Coseismic deformation from the 1999 Mw 7.1 Hector Mine, California, earthquake as inferred from InSAR and GPS observations, *Bull. Seismol. Soc. Am.*, *92*, 1,390–1,402, doi:10.1111/j.1365-246X.2010.04678.x, 2002.

Takeuchi, C., and Y. Fialko, Dynamic models of interseismic deformation and stress transfer from plate motion to continental transform faults, *J. Geophys. Res.*, *117*, B05403, doi:10.1029/2011JB009056, 2012.

Tse, S., and J. Rice, Crustal earthquake instability in relation to the depth variation of frictional slip properties, *J. Geophys. Res.*, *91*(B9), 9,452–9,472, 1986.